energies

Article

Establishment of CNN and Encoder–Decoder Models for the Prediction of Characteristics of Flow and Heat Transfer around NACA Sections

Janghoon Seo, Hyun-Sik Yoon * and Min-Il Kim

Department of Naval Architecture and Ocean Engineering, Pusan National University, 2 Busandaehak-ro 63beon-gil, Gumjeong-gu, Busan 46241, Republic of Korea
* Correspondence: lesmodel@pusan.ac.kr

Abstract: The present study established two different models based on the convolutional neural network (CNN) and the encoder–decoder (ED) to predict the characteristics of the flow and heat transfer around the NACA sections. The established CNN predicts the aerodynamic coefficients and the Nusselt number. The established ED model predicts the velocity, pressure and thermal fields to explain the performances of the aerodynamics and heat transfer. These two models were trained and tested by the dataset extracted from the computational fluid dynamics (CFD) simulations. The predictions mostly matched well with the true data. The contours of the velocity components and the pressure coefficients reasonably explained the variation of the aerodynamic coefficients according to the geometric parameter of the NACA section. In order to physically interpret the heat transfer performance, more quantitative and qualitative information are needed owing to the lack of the correlation and the resolution of the thermal fields. Consequently, the present approaches will be useful to design the NACA section-based shape giving higher aerodynamic and heat transfer performances by quickly predicting the force and heat transfer coefficients. In addition, the predicted flow and thermal fields will provide the physical interpretation of the aerodynamic and heat transfer performances.

Keywords: convolutional neural network; encoder–decoder; aerodynamics; heat transfer; NACA section; computational fluid dynamics

check for updates

Citation: Seo, J.; Yoon, H.-S.; Kim, M.-I. Establishment of CNN and Encoder–Decoder Models for the Prediction of Characteristics of Flow and Heat Transfer around NACA Sections. *Energies* **2022**, *15*, 9204. https://doi.org/10.3390/en15239204

Academic Editor: Maria Grazia De Giorgi

Received: 31 October 2022
Accepted: 30 November 2022
Published: 5 December 2022

1. Introduction

The NACA sections have been widely used in diverse applications, such as aircraft wings, the cross section of propellers, fans, ducts, and wind power generator blades. In addition, there are many studies using NACA sections in the area of biomimicry, microflow, and micro-air vehicles (MAVs) operating at a low Reynolds number (Re). Previous research [1–3] addressed aerodynamic bodies operating at low Re with conventional airfoils. Recently, Winslow et al. [4] briefly reviewed the Reynolds number effect on the aerodynamic performance of the airfoils by considering a wide range of Re. Winslow et al. [4] also systematically investigated the performance of airfoils and their sensitivities to geometric variations, such as camber and thickness in the wide range of Re, including low Re.

It is important to evaluate aerodynamic and heat transfer performances for the design and improved performance of the NACA sections [5–9]. The flow and thermal fields are needed to explain the physical interpretation of the aerodynamic performance. These are generally obtained by the CFD or the experimental fluid dynamics (EFD). However, the CFD and EFD are expensive and require the time and facilities to generate many accurate data. Therefore, there are needs for efficient and accurate methods and capabilities to process and use the data.

Recently, some studies have proposed deep learning techniques based on artificial intelligence to predict the aerodynamic coefficients and flow fields. Yilmaz and German [10] introduced the CNN model to predict the pressure coefficient (C_p) curve for inputs of airfoil surface coordinates. Additionally, the accuracy of the CNN model was improved by adjusting the hyperparameters of the CNN model and the distance of points on the airfoil surface. Zhang et al. [11] predicted lift coefficients using the multilayer perceptron (MLP)-based CNN model from the input image of airfoils. Sekar et al. [12] introduced a method to inversely design the two-dimensional airfoil using a deep CNN based on the surface pressure coefficient distribution. The predicted airfoil matched well with the true one.

Bhatnager et al. [13] proposed the shared ED model for the prediction of flow field. They applied the signed distance function to input data, which is a similar approach to the distance map by Duru et al. [14]. The pressure and velocity fields around airfoils were predicted by the trained shared ED model. The results showed that the proposed model was more efficient compared to separated alternatives, and the capability was assessed for unseen airfoil shapes. Chen et al. [15] introduced a graphical prediction method based on CNN for multiple aerodynamic coefficients of airfoils. The model of Chen et al. [15] simultaneously predicted the drag, lift, and pitch-moment coefficients from an airfoil image. They showed that their approach was more suitable to big data than the kriging method. Portal-Porras et al. [16] utilized two CNN models to investigate the effect of microtab and Gurney flap added on the trailing edge of the airfoil as a flow control device. Their CNN models had the capability to predict accurate characteristics of flow near the flow control device and the aerodynamic coefficients.

In the field of the heat transfer, increasing studies have used CNN to predict the characteristics of the heat transfer [17–19]. However, regarding to the NACA sections, the studies proposing the CNN model and its prediction capability of the thermal fields and the Nusselt number remain limited. Recently, Du et al. [20] applied a CNN framework for airfoil design optimization and prediction performance. They predicted the physical fields and the aerodynamic coefficients to optimize the airfoil shape. However, temperature was considered merely as one of the physical fields to examine the prediction capability of their model. Furthermore, the Nusselt number as a thermal performance was unpredicted.

As mentioned above, it is difficult to find research that simultaneously addresses the prediction of the force coefficient as the aerodynamic performance and the Nusselt number as the heat transfer efficiency. Furthermore, research is limited with regard to the simultaneous prediction of the flow and thermal fields to physically interpret the variation of the aerodynamic and heat transfer performance using CNN-based approaches.

Therefore, the purpose of the present study is to establish two different models to predict the characteristics of the flow and heat transfer around the NACA sections. One model is established based on the CNN to predict the aerodynamic coefficients and the Nusselt number. The other model is developed based on the encoder–decoder CNN approach to predict the velocity, pressure, and thermal fields to physically interpret the aerodynamic and heat transfer performance. The CFD is adopted to generate the dataset for the training and testing of the models. The various architectures of the two models are examined to identify their prediction performance. The geometric dependence of the prediction performance of the established models are tested by considering the various NACA section parameters. The predictive performance of the established CNN and ED models are assessed both quantitatively and qualitatively by the mean absolute percentage error and the contours of the absolute difference, respectively.

2. Methodology

The procedure of training and testing of the deep learning models is as follows. First, the dataset of the NACA section is prepared by CFD simulations. The CNN model is trained using input data of the image of the NACA section and the output label of drag and lift coefficients and Nusselt numbers. Simultaneously, the ED model is trained with the same input data as CNN model and the output label of distributions of velocities, pressure, and temperature. Finally, the trained CNN and ED models are tested by comparing the predicted results and the true ones.

2.1. Preparation of Dataset by CFD

The 561 NACA sections were chosen with the range of thickness (%) of 10–30, maximum camber position (%) of 0–6, and maximum camber (%) of 0–9. In many previous studies [10,12,14,15], 80% and 20% of the dataset were used as the training and test data, respectively. Thus, the present study uses the same ratios of 80% and 20% of the dataset for training and testing, respectively, resulting in 471 and 90 NACA sections for training and testing. These NACA sections were randomly selected.

2.2. Governing Equations

The present study considers the steady two-dimensional incompressible viscous conditions to define the flow and thermal fields around the NACA section. The governing equations are the continuity, Navier–Stokes, and energy equation, as follows.

$$\frac{\partial u_i}{\partial x_i} = 0 \tag{1}$$

$$\frac{\partial}{\partial x_j}(\rho u_i u_j) = -\frac{\partial p}{\partial x_i} + \frac{\partial}{\partial x_j}\left[\mu\left(\frac{\partial u_i}{\partial x_j} + \frac{\partial u_j}{\partial x_i}\right)\right] \tag{2}$$

$$\frac{\partial u_j T}{\partial x_j} = \frac{k}{\rho c_p}\frac{\partial^2 T}{\partial {x_j}^2} \tag{3}$$

where x_i, u_i, ρ, p, μ, k and c_p are Cartesian coordinates, corresponding velocity components, density, pressure, viscosity, thermal conductivity, and specific heat, respectively. The semi-implicit method for the pressure-linked equation (SIMPLE) algorithm is used to address the pressure-velocity coupling and the overall solution procedure by using an iterative solution approach, which was introduced by Patankar and Spalding [21]. The second-order scheme was adopted for convection and pressure terms. A second-order central difference scheme was adopted for diffusion terms. A convergence criterion of 10^{-6} was used in our simulations. Further details of the implementation can be found in the STAR CCM+ manuals [22].

2.3. Computational Domain and Boundary Conditions

Figure 1 shows the boundary conditions and computational domain. A fixed Cartesian coordinate (x,y) with the origin at the wing tip is adopted. The x-axis is parallel to the inlet flow direction. The length and height of the computational domain are 25c and 16c, respectively. A uniform flow was used on the inlet boundary, and the convective condition ($a\partial u_i/\partial x_i = 0$) was imposed at the outlet, where a is the space-averaged streamwise velocity at the outlet [23,24]. The no-slip condition was imposed on the surface of the NACA section, and the far-field boundary was considered as the symmetry condition, as shown in Figure 1. A Neumann condition was applied for the pressure boundary. For the temperature boundaries, a constant temperature was imposed on the inflow boundary, and a convective condition was applied at the outflow boundary. A constant temperature was applied on the walls.

The Reynolds number ($Re = \rho U_\infty c/\mu$) of 1000 and Prandtl number ($Pr = c_p\mu/k$) of 0.7 were considered, with a angle of attack of 0°.

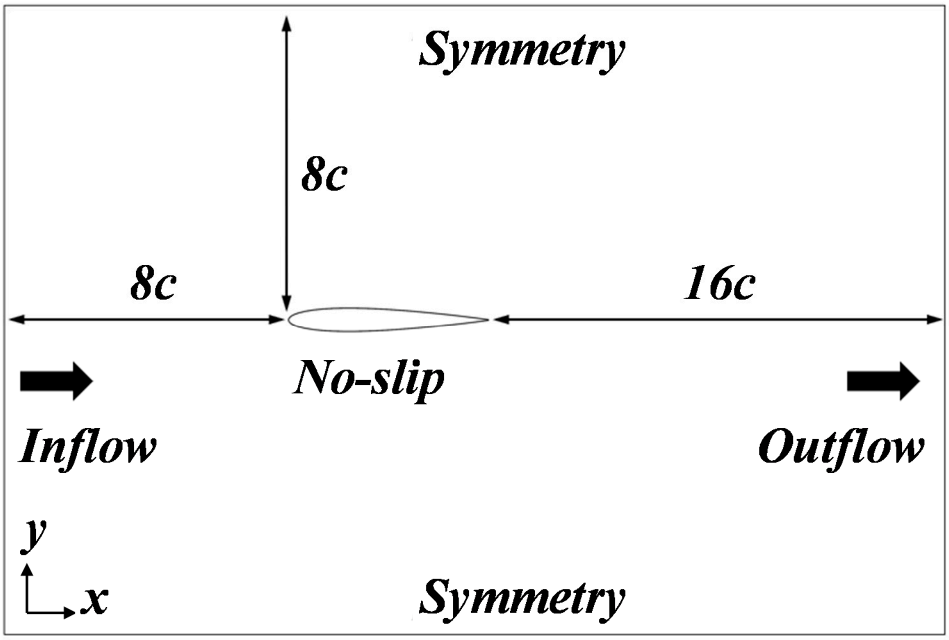

Figure 1. Schematic of computational domain and boundary conditions.

2.4. Grid System and Validation

The present grid system is presented in Figure 2, where the grid distribution near the NACA section is inserted. The grid is smoothly stretched from the airfoil surface. In order to evaluate the grid dependence, three different grid systems are generated by applying the grid-refinement ratio of $\sqrt{2}$. Table 1 reports the results of the grid dependence test for three grid systems for NACA 0012 at $\alpha = 0°$. The differences between the results of the three grid systems are within 1%. Therefore, the medium grid system is selected for all computations.

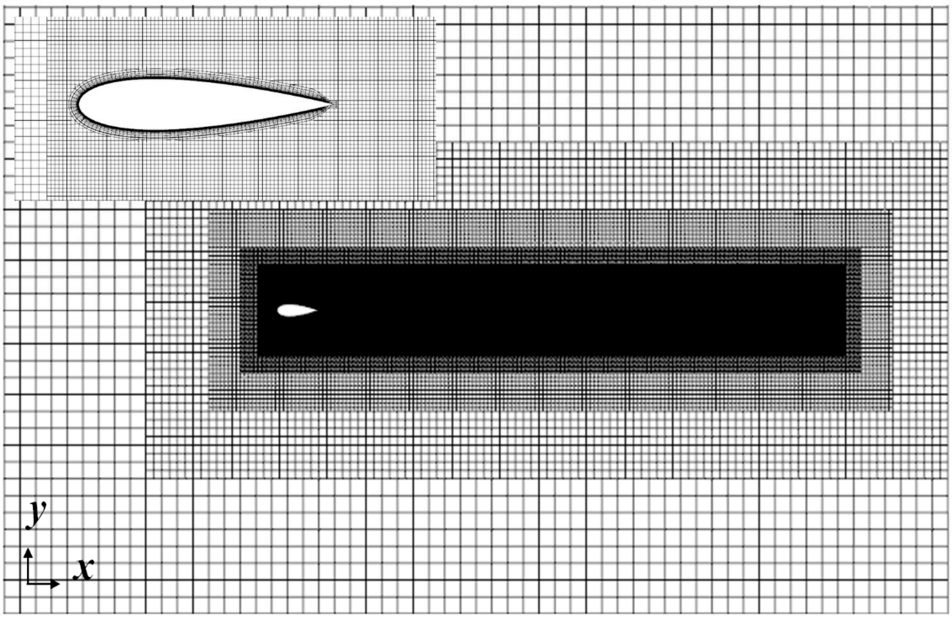

Figure 2. The grid system of the NACA section.

Table 1. Grid dependency test for NACA 0012 at $\alpha = 0\,^{\circ}$.

Case	Number of Volumes	C_D	Difference (%)
Coarse	58,006	0.1253	−0.31
Medium	128,201	0.1256	
Fine	192,302	0.1257	0.24

The present numerical methods are validated by comparing the present results with previous results [25,26], as seen in Table 2. The present aerodynamic coefficients and Nusselt number are similar with previous results [25,26].

Table 2. Comparison of aerodynamic coefficients and Nusselt number with previous data for the NACA 0012 at $\alpha = 0\,^{\circ}$ and 10°.

Case	α(°)	C_D	C_L	Nu
Kurtulus [25]	0	0.1207	0.0	
Shrestha [26]		-	-	18.953
Present		0.1256	0.0	19.415
Kurtulus [25]	10	0.1649	0.4173	
Present		0.1682	0.4123	

3. Deep Learning Model

3.1. CNN Model

In the present paper, the CNN model using Tensorflow [27] is considered for the prediction of drag and lift coefficients and Nusselt number. LeCun et al. [28] first introduced the CNN model to improve the performance by significantly reducing the trainable parameters, resulting in the CNN model becoming a representative deep learning model. The convolutional, pooling, and fully connected layers compose the typical CNN model architecture, as presented in Figure 3a. This architecture can also be divided as classification and feature extraction. Convolutional and max pooling layer are applied to extract features of input images, and hidden layers are fully connected with weights and bias. In the feature extraction, the convolution layer-I and -II are convolved from the input and the convolution layer-I, respectively. The pooling layer-I and -II are pooled from the convolution layer-I and -II, respectively. Two fully connected layers of I and II are involved in the classification, which classify the images. The images become a flattened array by converting the two-dimensional array of the previous convolved and pooled layers to a one-dimensional array.

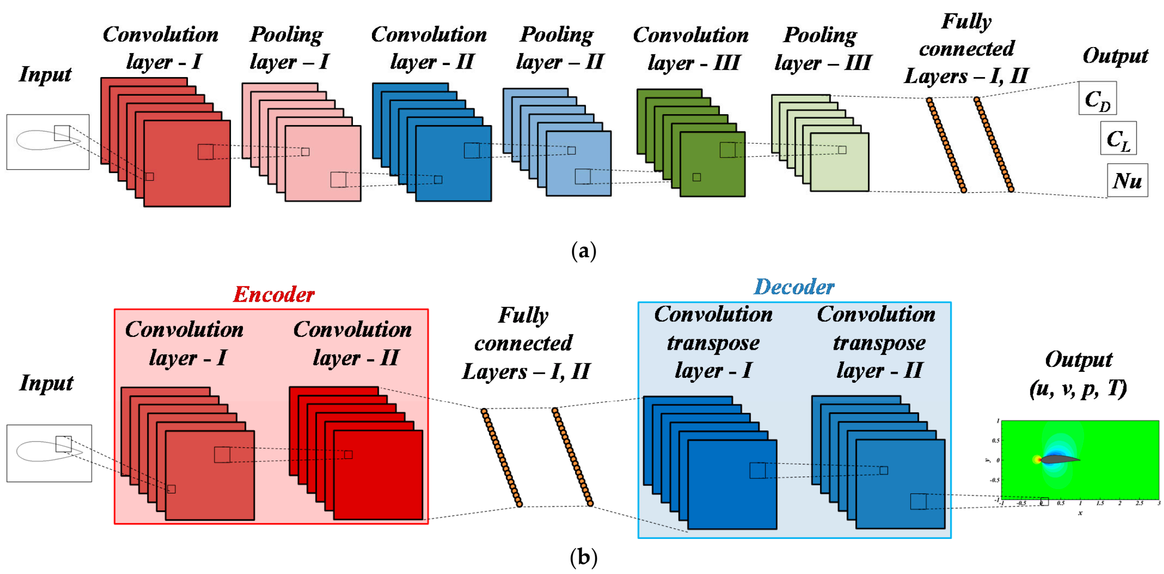

Figure 3. Typical layer architectures of (**a**) CNN and (**b**) ED models.

3.2. ED Model

In addition to CNN, an ED model coded Tensorflow [27] is adopted to learn the mapping of an input NACA section and the output of flow and thermal fields. In contrast to the convolution layers, which are used to separate the input and extract feature maps, the transposed convolution layers are adopted to build an output from those feature maps, as shown in Figure 3b.

The ED models were validated to operate well for the image transformation [10]. Thus, the present study adopts the ED model to formulate problems as an image transformation task. The encoder part consists of the convolution layer-I and the convolution layer-II to encode the extracted feature by using hierarchical representation of the input images. Two fully connected layers of I and II are employed for the classification. The convolution transpose layers-I and -II are used to decode output labels by using extracted features. The number of blocks in the encoder part and the decoder part is identical, and each block is composed of the same number of layers: convolutional or transpose convolutional layer and an ReLU (Rectified linear unit) activation unit, excepting the output blocks. All convolution and transposed convolution operations are operated with a 3×3 filter size. Figure 3b shows the proposed ED architecture.

4. Results and Discussion

4.1. Training of CNN and ED Models

The processes of CNN and ED trainings are comparable to those of the optimization, which is realized by the minimization of the mean square error (MSE). The training is performed using ADAM [29] and the backpropagation algorithm [28,30].

The main purpose of the training process is the minimization of the loss function. The present study considers MSE as the loss function. The MSE is defined by the difference between the true data and the CNN model prediction, as follows:

$$MSE = \frac{1}{N}\sum_{i=1}^{N}(Pd_i - Tr_i)^2 \tag{4}$$

where Pd is the output predicted by the model, Tr is the true output, and N is the number of data points. Normalization is performed to output features such that the output values are in between -1 to 1. In other respects, normalization is not required for the input images, as the pixel values ranges from 0 to 1.

The numbers of the pooling, fully connected, and convolutional layers can be flexibly chosen according to the problem complexity. Hence, the diverse architectures of the CNN model are evaluated by considering different numbers of the fully connected and convolutional layers.

The three different layer numbers of 1, 3, and 5 are considered as the convolution layer. In addition, the three fully connected layer numbers of 1, 2, and 3 are considered in this study. The CNN model architectures are designed by the combinations of convolution and fully connected layers with different layer numbers in Table 3. These CNN model architectures are plotted in Figure 3a.

Table 3. Parameters for CNN model.

CNN Model	Convolution Layers	Fully Connected Layers
CA-1C2F	1	2
CA-3C2F	3	2
CA-5C2F	5	2
CA-3C1F	3	1
CA-3C5F	3	3

First, the effect of the convolution layer number on the training of the CNN model is studied by considering the three convolutional layers of CA-1C2F, CA-3C2F, and CA-5C2F, where F and C are the fully connected and convolution layers, respectively. In this test of the dependence of the convolution layer number, the number of the fully connected layers is fixed as two.

The time evolutions of the MSE for three convolution layers present no considerable difference in convergence, as presented in Figure 4. Thus, the number of convolution layers of three is selected to evaluate the impact of the fully connected layer number on the error convergence by considering smaller and larger numbers of 1 and 5 rather than 3. As a result, three fully connected layers of CA-3C1F, CA-3C2F, and CA-3C3F give a similar validation and training of the MSE convergence, as shown in Figure 4. Eventually, the CNN model architectures adopted in the present research provide a saturated MSE with about the same error convergence. As a result, the CA-3C2F is chosen for further study. The training is stopped after 1000 epochs, when the MSE is no longer significantly reduced. The MSE becomes small to less than 5.0×10^{-5}.

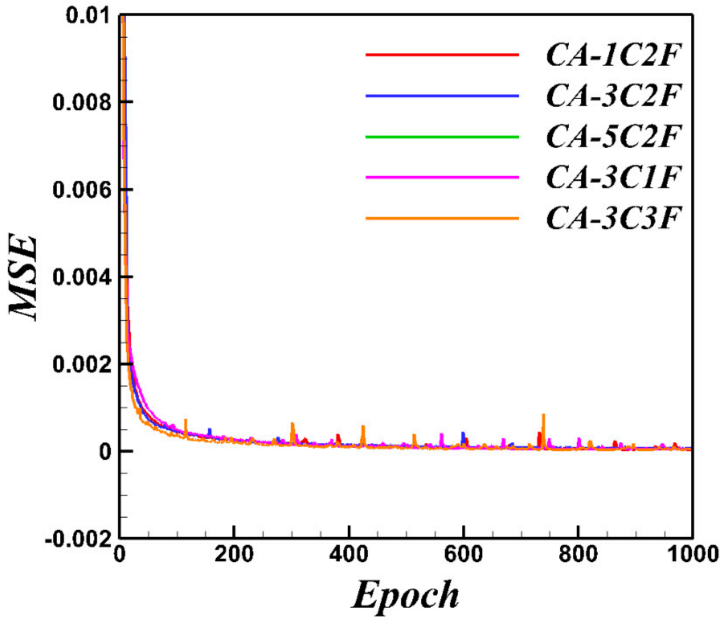

Figure 4. Convergence histories of MSE with different number of layers for CNN model.

In order to establish the encoder–decoder network architecture to correctly predict the velocity vectors, pressure, and thermal fields around different NACA sections, the effect of the hyperparameters in the encoder–decoder network architecture on the convergence is evaluated by estimating the MSE according to the epoch. As mentioned for the ED model architecture, a network configuration is symmetrically constructed in the present research. Hence, the encoder and the decoder parts contain the same number of blocks. In addition, each block is composed of the same number of layers. The various ED model architectures are presented in Table 4, showing the three types of convolution and transposed convolutional layers. The convolution layers have 1, 3, and 5 numbers. The transposed convolutional layers have 1, 2, and 3 numbers

Table 4. Parameters for ED model.

ED Model	Convolution Layers and Convolutional Transpose Layers	Fully Connected Layers
ED-1C2F	1	2
ED-3C2F	3	2
ED-5C2F	5	2
ED-3C1F	3	1
ED-3C3F	3	3

The same procedure and layer numbers of the ED model with the CNN model are adopted for the evaluation of the error convergence. Therefore, first, with three fixed fully connected layers, three convolutional and transposed convolutional layers of ED-1C2F, ED-3C2F, and ED-5C2F are examined to identify their effect on the error convergence. The time series of the MSE for different convolution and transposed convolutional layers have no significant discrepancy in the convergence, as clarified in Figure 5. Thus, the medium layer numbers of three is selected as the number of convolutional and transposed convolutional layers; then, the effect of the fully connected layer number on the convergence of the error is assessed by considering two additional fully connected layers with the layer numbers of 1 and 5. Eventually, the ED model architectures considered in the present research provide a saturated MSE with similar error convergence. Therefore, ED-3C2F is chosen for further study.

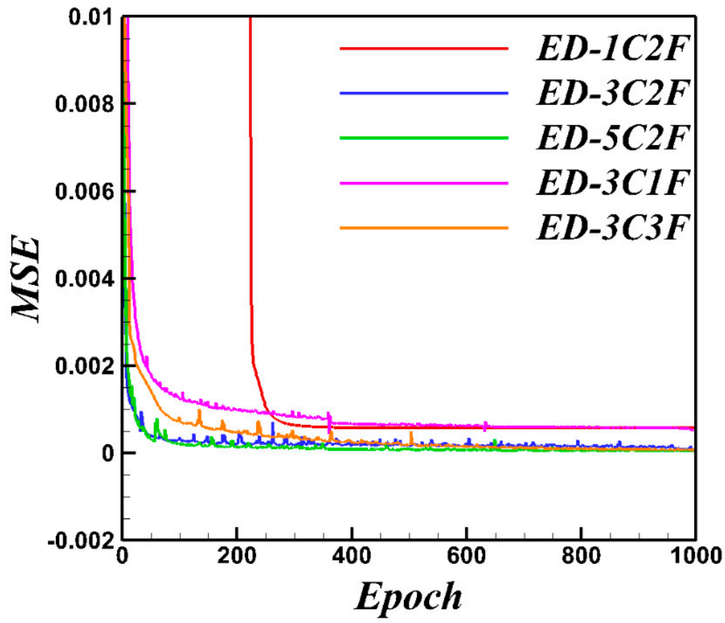

Figure 5. Convergence histories of MSE with different number of layers for ED model.

4.2. Prediction of Aerodynamic Coefficients and Nusselt Number

The accuracy performance of the established CNN model for predicting the aerodynamic (force coefficients) and thermal performance (Nusselt number) for the inputs of the NACA section surface image is evaluated by using the 200 NACA section samples corresponding to about 20% of the dataset. The drag and lift coefficients (C_D and C_L) are popularly used to assess the aerodynamic performance of the NACA section, and the Nusselt number (Nu) represents the thermal efficiency. Thus, the predicted C_D, C_L, and Nu are compared to the true values obtained by CFD simulations. The prediction accuracy of the established CNN model is presented by the scatter plots for C_D, C_L, and Nu, as shown in Figure 6.

Most predicted values of C_D, C_L, and Nu are clustered near the 45° line, as shown in Figure 6a–c, respectively. These distributions mean that the values predicted by the established CNN model are close to the true values obtained by the CFD.

The comparison of the CNN model predicted values and the true ones is performed for the various NACA section shapes covering the maximum camber, camber position, and thickness according to the designation of the NACA Section 4-digit series. Therefore, these scatter plots support the reliability of the accuracy performance of the established CNN model and the applicability, which is nearly independent of the NACA section shapes.

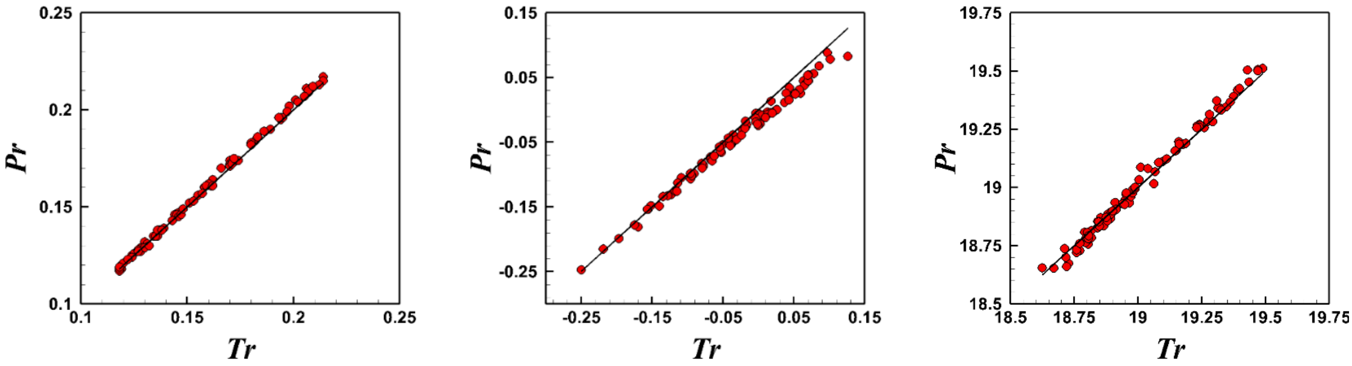

(**a**) (**b**) (**c**)

Figure 6. Comparison of true and predicted values: (**a**) C_D, (**b**) C_L, and (**c**) Nu.

4.3. Prediction of Flow and Thermal Fields

In order to select the NACA sections to examine the prediction performance of the established ED model predicting the flow and thermal fields, the combination of the parameters to define the NACA Section 4-digit series is utilized. As a result, four NACA sections of 2412, 5412, 2912, and 2430 are considered to evaluate the prediction capability of the ED model. The NACA 2412 is selected as the reference to compare the effect of the geometric parameter. The maximum camber of 2 is changed into 5 by considering NACA 5412. The position of the maximum camber increases from 4 to 9 by considering NACA 2912. The maximum thickness of 12 increases to 30 by adopting NACA 2430.

The flow fields of four NACA sections of NACA 2412, NACA 5412, NACA 2912, and NACA 2430 are presented as the contours of x- and y-directional velocities of u and v in Figures 7 and 8, respectively, where the predicted and true flow fields are compared and the error distributions are exhibited to determine the accuracy of the established ED model for flow field prediction. In general, the distributions of the predicted streamwise and vertical velocities are about the same as those of the true ones, regardless of the geometric parameters defining the NACA section, as shown in Figures 7 and 9.

The relatively large difference between the predicted and true streamwise velocities appears in the areas over the lower and upper surfaces, where the local large velocities occur and form steep gradients, as shown in Figure 7.

The variations of the maximum camber and its position have a minor effect on the error of the predicted streamwise velocities, as shown in Figure 7a–c for NACA 2412, 5412, and 2912, respectively. However, the maximum thickness of the NACA section gives a larger effect on the error of the predicted streamwise velocities, as shown in Figure 7d for NACA 2430.

The established ED model closely predicts the vertical velocity around the NACA section in comparison with true ones, regardless of the geometric parameter, as clarified in Figure 8. The distribution of the errors for the vertical velocity is consistent with that for the streamwise velocity. Namely, the large errors appear in the regions where the local large velocities occur and form steep gradients. Hence, the leading edge forms larger upward and downward vertical velocities, resulting in the appearance of the large errors in the region near leading edge. In particular, the large thickness of the NACA section forms a wider area of errors, as shown in Figure 8d for NACA 2430. Additionally, the trailing edge for the NACA sections with large thickness contributes great variation of the vertical velocity, leading to larger errors in region near the trailing edge. However, the established ED model is able to reliably predict the flow characteristics, and these errors are not considered significant.

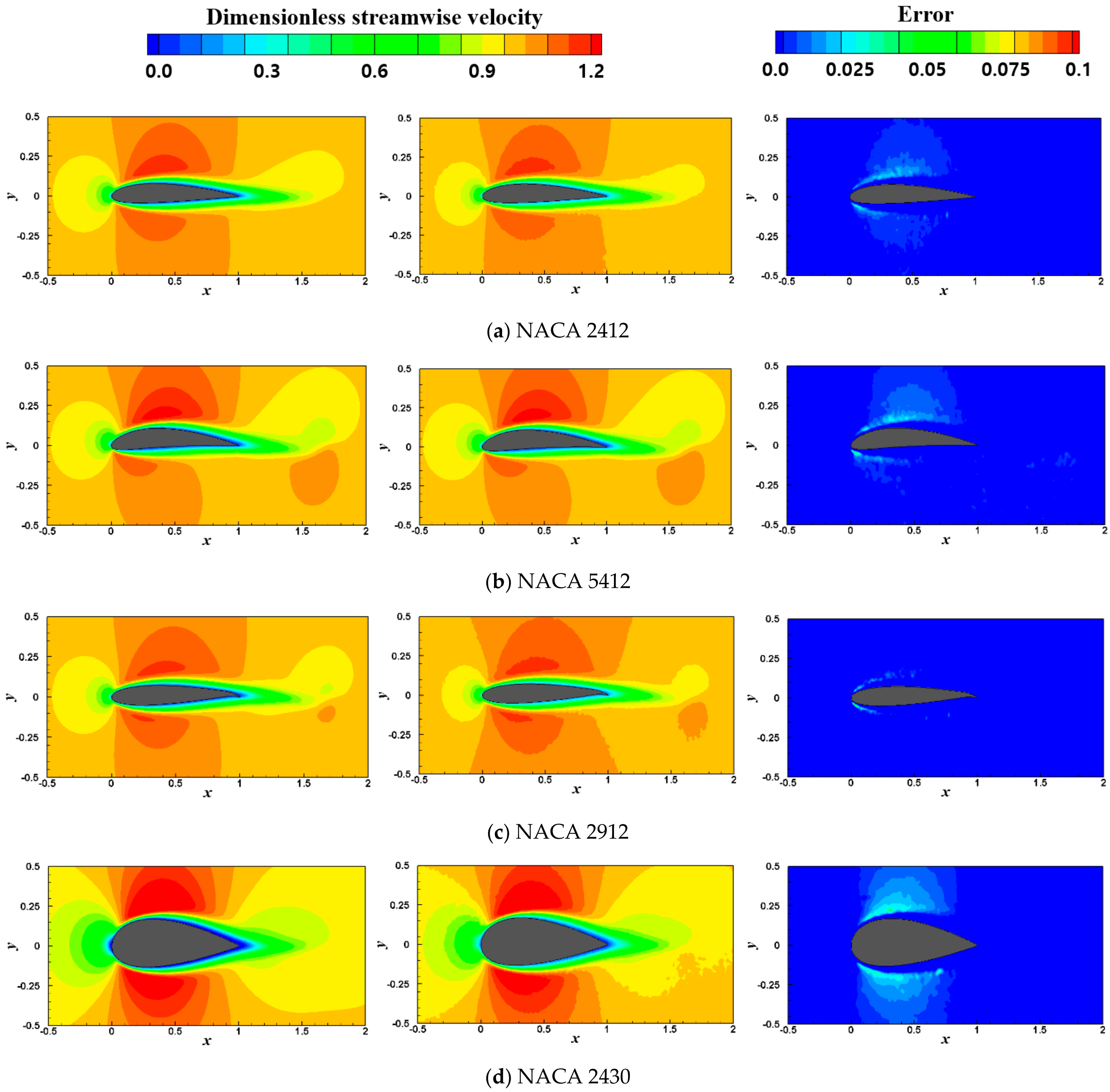

Figure 7. Contours of dimensionless streamwise velocity in the *x*-*y* plane for true values (**left column**), predicted values (**center column**), and error values (**right column**) for different NACA sections.

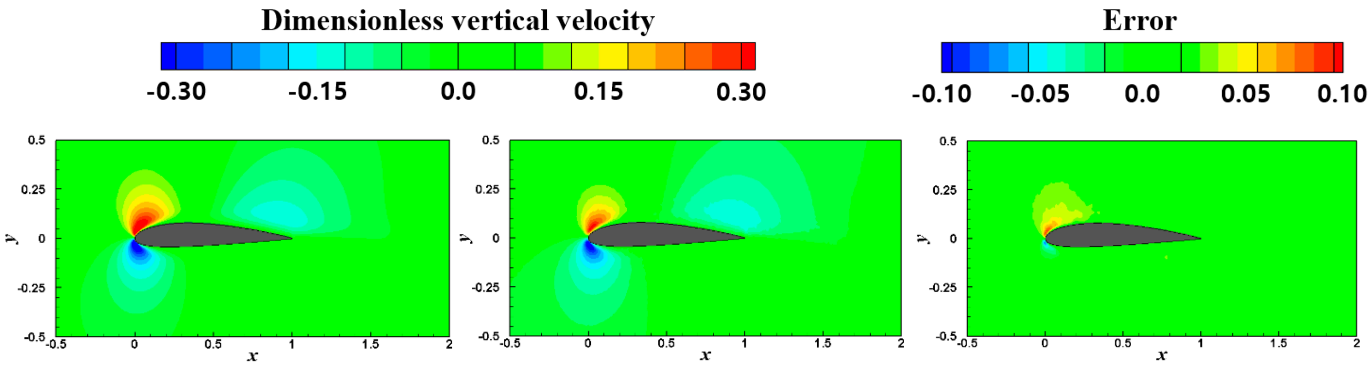

(**a**) NACA 2412

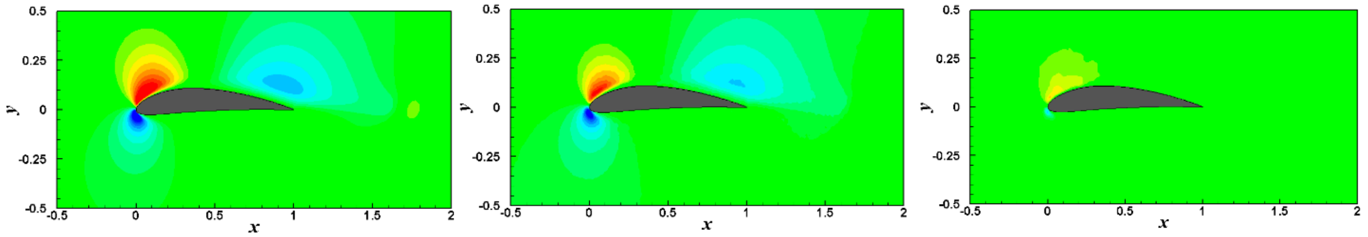

(**b**) NACA 5412

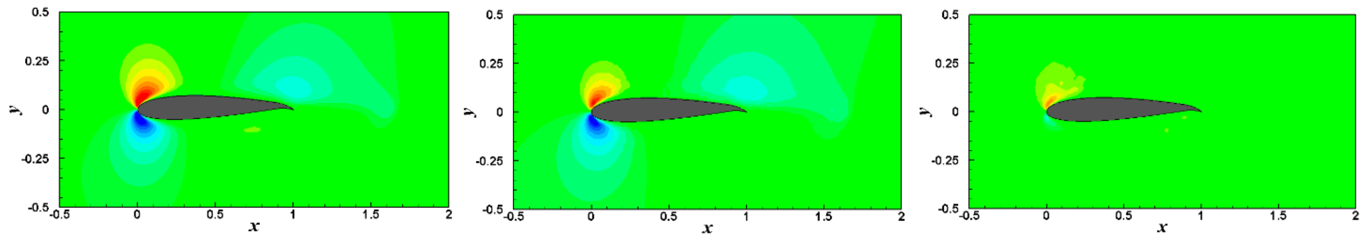

(**c**) NACA 2912

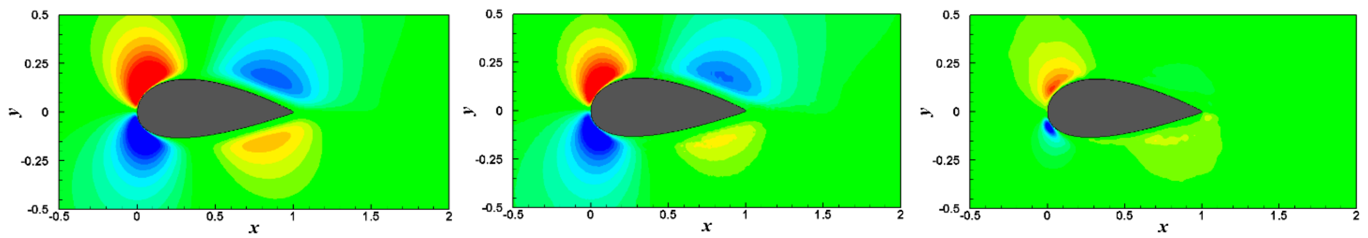

(**d**) NACA 2430

Figure 8. Contours of dimensionless vertical velocity in the *x*-*y* plane for true values (**left column**), predicted values (**center column**), and error values (**right column**) for different NACA sections.

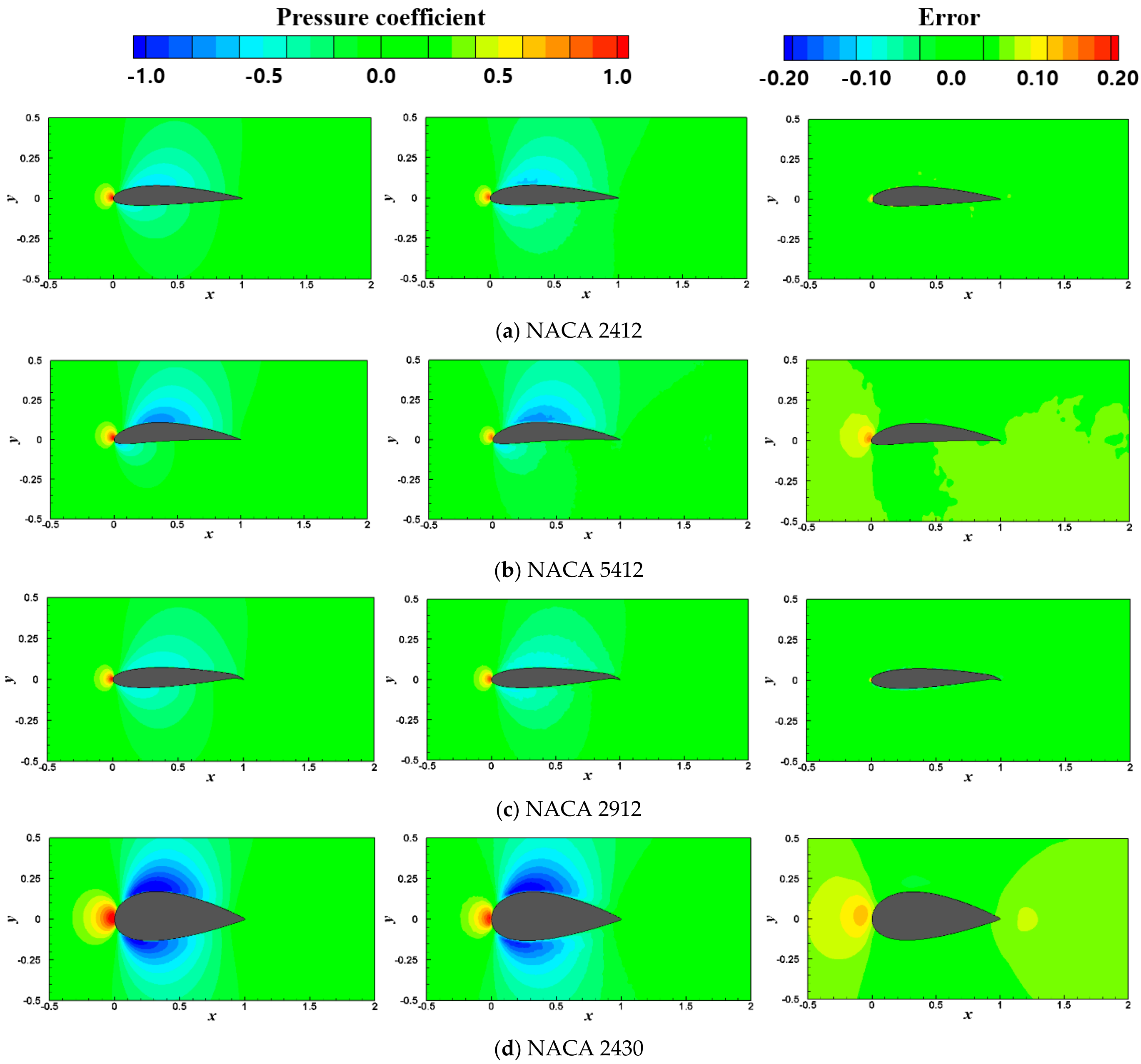

Figure 9. Contours of pressure coefficient in the x-y plane for true values (**left column**), predicted values (**center column**), and error values (**right column**) for different NACA sections.

The distributions of the pressure coefficients are strongly associated with the flow stagnation, acceleration, and deceleration over the surface. Therefore, the contours of the pressure coefficient for four NACA sections in Figure 9 can be comparable to those of the streamwise velocity in Figure 7. Additionally, the distributions of the pressure coefficients over the surface govern the aerodynamic coefficients of C_D and C_L. Thus, the predicted and true values of C_D and C_L for the four different NACA sections in Figure 10 also verify the reliability of the present CNN model.

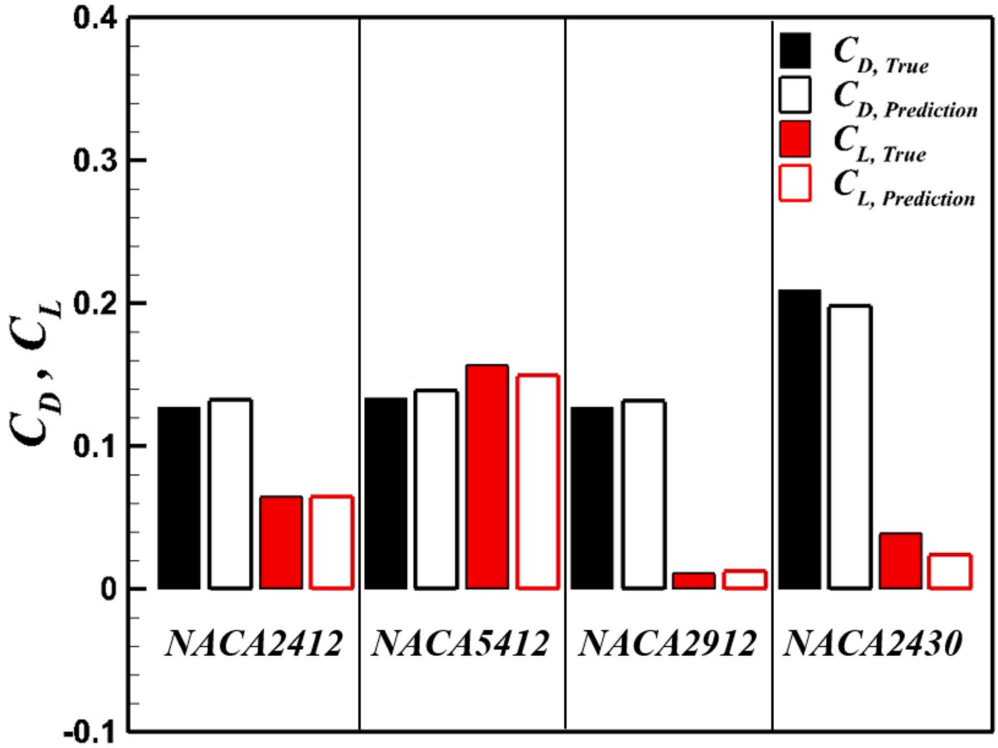

Figure 10. Comparison of drag and lift coefficients between true values and predicted values.

The highest pressure occurs at the stagnation point near the leading edge. The flow turns around and accelerates over the surface, forming a local high speed region, where the lowest pressure appears. NACA 2412 and 5412 form the maximum streamwise velocity over the upper surface, as shown Figure 9a,b, respectively. NACA 5412 forms larger and wider streamwise velocity over the upper surface than NACA 2412. Thus, NACA 5412 forms lower pressure in a wider area over the upper surface than NACA 2412. As a result, NACA 5412 gives larger C_L than NACA 2412, as shown in Figure 9a for NACA 2412 and Figure 9b for NACA 5412.

In the case of NACA 2912, where the position of the maximum camber is closer to the trailing edge, the pressure coefficients over the upper and lower surfaces reveal very similar distribution (see Figure 9c), since the streamwise velocities over the upper and lower surface are more symmetrically distributed than NACA 2412 and 5412, as shown in Figure 7. These predicted pressure and velocity fields give a reliable physic explanation for the C_L of NACA 2912, which is much smaller than that of NACA 2412 and 5412 in Figure 10.

As well known, as the thickness becomes large, the drag increases and the lift decreases. The present predicted C_D and C_L of NACA 2430 are larger and smaller than those of the NACA 2412, respectively, as shown in Figure 10. This thickness effect on the aerodynamic coefficients is clearly supported by the pressure distributions in Figure 9, where high pressure is widely distributed near the leading edge.

The predicted and true thermal fields with dimensionless temperatures for four NACA sections are compared in Figure 11. In addition, the predicted Nusselt numbers by the present CNN model and the true ones are presented in Figure 12. Regardless of the geometric parameters, the present ED model closely predicts the isothermal distributions near the NACA sections as compared to those of the true results.

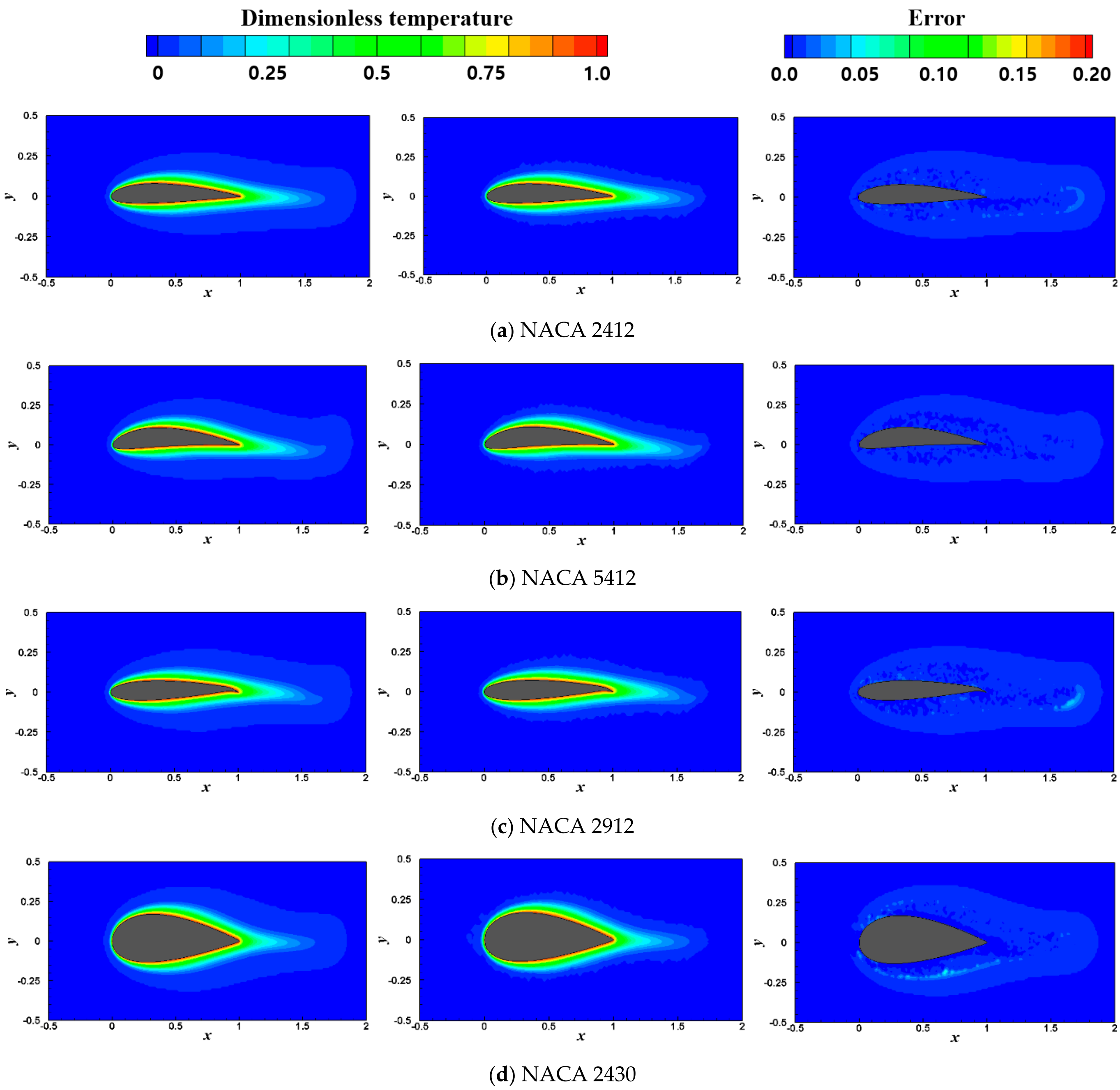

Figure 11. Contours of dimensionless temperature in the *x*-*y* plane for true values (**left column**), predicted values (**center column**), and error values (**right column**) for different NACA sections.

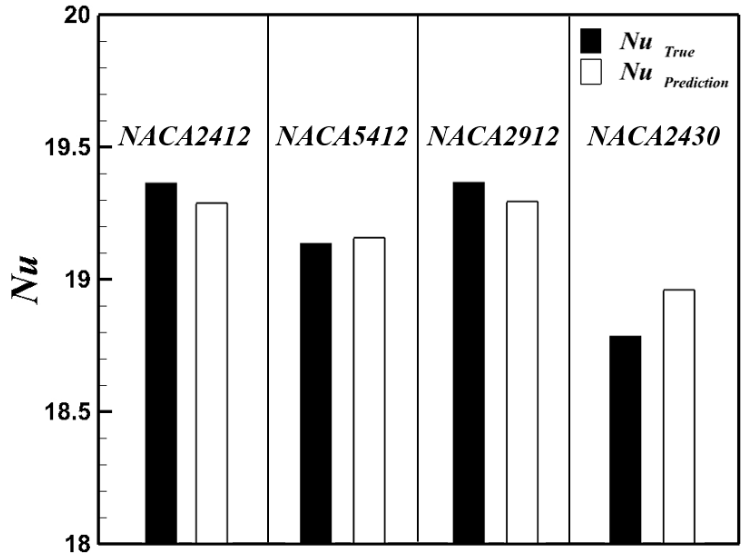

Figure 12. Comparison of Nusselt numbers between true values and predicted values.

The present study considers the forced convection, which is governed by the fluid flow. Thus, it can be expected that the flow fields and the aerodynamic coefficients can explain the thermal field, which determines the Nusselt number. Although the predicted flow and thermal fields closely represent the true ones, it seems that the contours of velocities, pressure, and temperature are not enough to explain the variation of the Nusselt number according to the geometric parameter of the NACA section. It is difficult to find the correlation between the aerodynamic coefficients and the Nusselt number for the NACA sections in Figures 10 and 12. Additionally, it is difficult to clearly identify the thermal gradients on the wall based on the predicted isothermal contours near the NACA section in Figure 11. Thus, in order to physically interpret the heat transfer performance of the NACA sections, more quantitative and qualitative information, such as the high resolved thermal variation in the vicinity of the surface and the local viscous and pressure components of the aerodynamic coefficients, are needed to define the correlation to the Nusselt number.

The percentage of data points to the total data points is presented according to the cumulative percentage of absolute error in Figure 13. More than 80% of data points have less than 10% deviation from the true values, as shown in Figure 13. About 3.5% of data points have more than 100% error; these can be considered as outliers. Nevertheless, these data points with large errors appear in the predicted u, v pressure coefficient and thermal fields in Figures 8–10, and 12. Generally, these data points with large errors are distributed near the surface of the NACA, section where the predicted values form a very sharp gradient, leading to possible misinterpretation of a quantitative assessment of the present established model. Generally, the mean absolute percentage error is simply used as the measurement of the prediction accuracy. The present ED model achieves an overall accuracy of approximately 87%.

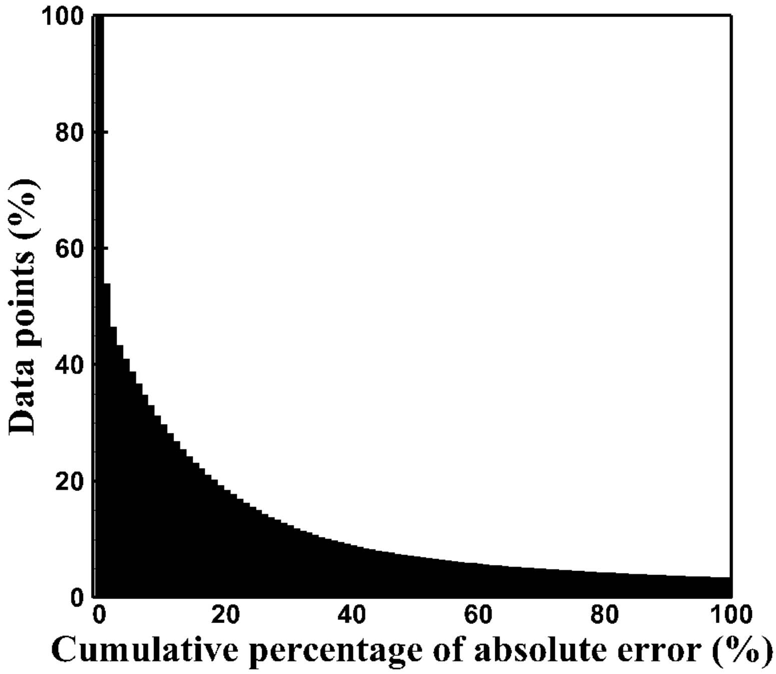

Figure 13. Distributions of data points with cumulative percentage of absolute error for ED model.

5. Conclusions

The present study established two different deep learning models to predict the characteristics of the fluid flow and heat transfer around the NACA sections. One established model based on the CNN is utilized to predict the aerodynamic coefficients of C_D and C_L as the aerodynamic performance and the Nusselt number as the indication of the force heat transfer performance. The other model based on the encoder–decoder CNN approach was established to predict the velocity, pressure, and thermal fields. These flow and thermal fields were predicted to explain the performances of the aerodynamic and heat transfer. These two models were trained and tested by the dataset extracted from the CFD simulations.

The various architectures of CNN and ED models were constructed by using different numbers of the fully connected and convolutional layers. These architectures of CNN and ED models were assessed by the convergence histories of MSE. The scatter plot of the prediction accuracy for the test set identified that the values predicted by the CNN model are very similar to the actual values.

The predictive performance of the established ED model was assessed both quantitatively and qualitatively by the absolute difference contours and the mean absolute percentage error, respectively. The flow and thermal fields of the velocity components, the pressure coefficients, and the temperature between the ED model prediction and the truth were evaluated by the absolute difference contour plots. The predictions mostly matched well with the true data. However, relatively large errors appeared in regions where the sharp gradients of each dependent variable occurred, near the leading edge and over the surfaces containing the maximum and minimum. Thus, a highly resolved and larger dataset are needed to improve the prediction capability of the ED model.

The contours of the velocity components and the pressure coefficients reasonably explained the variation of the aerodynamic coefficients of C_D and C_L for different geometric parameters of the NACA section. However, the contours of velocities, pressure, and temperature were not adequate to explain the variation of the Nusselt number according to the geometric parameter of the NACA section, owing to the lack of the correlation between the force coefficients and the Nusselt number, and the insufficient resolution of the isotherms to clearly identify the temperature gradients. Thus, in order to physically interpret the heat transfer performance, more quantitative and qualitative information, such as the high resolved temperature variation in the vicinity of the surface and the local viscous and pressure components of the force coefficients, are needed to define the correlation to the Nusselt number.

Consequently, the present approaches will be valuable to design the NACA section–based shape, giving higher aerodynamic and heat transfer performances by quickly predicting the force and heat transfer coefficients. In addition, the predicted flow and thermal fields will provide the physical interpretation of the aerodynamic and heat transfer performances.

The present study presents the performance of the CNN and ED models through prediction of the characteristics of the two-dimensional flow and heat transfer around the airfoils. It implies that the deep learning model may be applied to predict the performance of three-dimensional airfoils with different shapes and Reynolds numbers. Therefore, the prediction of aerodynamic performance for three-dimensional airfoils with different Reynolds numbers and various shapes can be a promising research area in the future.

Author Contributions: Conceptualization, J.S.; writing—original draft preparation, J.S.; writing—review and editing, H.-S.Y.; supervision, H.-S.Y.; software, M.-I.K.; validation, M.-I.K. All authors have read and agreed to the published version of the manuscript.

Funding: This work was supported by the National Research Foundation of Korea (NRF) grant funded by the Korea government (MSIT) through NRF-2019R1A2C1009081.

Institutional Review Board Statement: Not applicable.

Informed Consent Statement: Not applicable.

Data Availability Statement: Not applicable.

Conflicts of Interest: The authors declare no conflict of interest.

References

1. Shrestha, R.; Benedict, M.; Hrishikeshavan, V.; Chopra, I. Hover Performance of a Small-Scale Helicopter Rotor for Flying on Mars. *J. Aircr.* **2016**, *53*, 1160–1167. [CrossRef]
2. McMasters, J.H.; Henderson, M.L. Low Speed Single-Element Airfoil Synthesis. NASA. Langley Res. Center The Sci. and Technol. of Low Speed and Motorless Flight. 1979. Available online: https://ntrs.nasa.gov/citations/19790015719 (accessed on 25 November 2022).
3. Mueller, T.J. Aerodynamic Measurements at Low Reynolds Numbers for Fixed Wing Micro-Air Vehicles. RTO AVT/VKI Special Course on Development and Operation of UAVs for Military and Civil Applications. 1999. Available online: http://www.dtic.mil/docs/citations/ADP010760 (accessed on 25 November 2022).
4. Winslow, J.; Otsuka, H.; Govindarajan, B.; Chopra, I. Basic Understanding of Airfoil Characteristics at Low Reynolds Numbers (10^4–10^5). *J. Aircr.* **2018**, *55*, 1050–1061. [CrossRef]
5. Meng, X.; Hu, H.; Li, C.; Abbasi, A.A.; Cai, J.; Hu, H. Mechanism study of coupled aerodynamic and thermal effects using plasma actuation for anti-icing. *Phys. Fluids* **2019**, *31*, 037103. [CrossRef]
6. Cheriet, N.; Amirat, H.; Korichi, A.; Polidori, G. Conjugate heat transfer enhancement over heated blocks using airfoil deflectors. *Therm. Sci. Eng. Prog.* **2021**, *25*, 101011. [CrossRef]
7. Zhang, H.; Guo, J.; Cui, X.; Zhou, J.; Huai, X.; Zhang, H.; Han, Z. Experimental and numerical investigations of thermal-hydraulic characteristics in a novel airfoil fin heat exchanger. *Int. J. Heat Mass Transf.* **2021**, *175*, 121333. [CrossRef]
8. Ho, J.Y.; Wong, K.K.; Leong, K.C.; Wong, T.N. Convective heat transfer performance of airfoil heat sinks fabricated by selective laser melting. *Int. J. Therm. Sci.* **2017**, *114*, 213–228. [CrossRef]
9. Chu, W.X.; Li, X.H.; Ma, T.; Chen, Y.T.; Wang, Q.W. Study on hydraulic and thermal performance of printed circuit heat transfer surface with distributed airfoil fins. *Appl. Therm. Eng.* **2017**, *114*, 1309–1318. [CrossRef]
10. Yilmaz, E.; German, B. A convolutional neural network approach to training predictors for airfoil performance. In Proceedings of the 18th AIAA/ISSMO Multidisciplinary Analysis and Optimization Conference, Denver, CO, USA, 5–9 June 2017.
11. Zhang, Y.; Sung, W.J.; Mavris, D.N. Application of convolutional neural network to predict airfoil lift coefficient. In Proceedings of the 2018 AIAA/ASCE/AHS/ASC Structures, Structural Dynamics, and Materials Conference, Kissimmee, FL, USA, 8–12 January 2018.
12. Sekar, V.; Zhang, M.; Shu, C.; Khoo, B.C. Inverse Design of Airfoil Using a Deep Convolutional Neural Network. *AIAA J.* **2019**, *57*, 933–1003. [CrossRef]
13. Bhatnagar, S.; Afshar, Y.; Pan, S.; Duraisamy, K.; Kaushik, S. Prediction of aerodynamic flow fields using convolutional neural networks. *Comput. Mech.* **2019**, *64*, 525–545. [CrossRef]

14. Duru, C.; Alemdar, H.; Baran, Ö.U. CNNFOIL: Convolutional encoder decoder modeling for pressure fields around airfoils. *Neural Comput. Appl.* **2021**, *33*, 6835–6849. [CrossRef]
15. Chen, H.; Weiqi, Q.; Song, W. Multiple Aerodynamic Coefficient Prediction of Airfoils Using a Convolutional Neural Network. *Symmetry* **2020**, *12*, 544. [CrossRef]
16. Portal-Porras, K.; Fernandez-Gamiz, U.; Zulueta, E.; Ballesteros-Coll, A.; Zulueta, A. CNN-based flow control device modelling on aerodynamic airfoils. *Sci. Rep.* **2022**, *12*, 8205. [CrossRef] [PubMed]
17. Seo, Y.M.; Pandey, S.; Lee, H.U.; Choi, C.; Park, Y.G.; Ha, M.Y. Prediction of heat transfer distribution induced by the variation in vertical location of circular cylinder on Rayleigh-Bénard convection using artificial neural network. *Int. J. Mech. Sci.* **2021**, *209*, 106701. [CrossRef]
18. Edalatifar, M.; Tavakoli, M.B.; Ghalambaz, M.; Setoudeh, F. Using deep learning to learn physics of conduction heat transfer. *J. Therm. Anal. Calorim.* **2021**, *146*, 1435–1452. [CrossRef]
19. Kim, D.J.; Kim, S.I.; Kim, H.S. Thermal simulation trained deep neural networks for fast and accurate prediction of thermal distribution and heat losses of building structures. *Appl. Therm. Eng.* **2022**, *202*, 117908. [CrossRef]
20. Du, Q.; Liu, T.; Yang, L.; Li, L.; Zhang, D.; Xie, Y. Airfoil design and surrogate modeling for performance prediction based on deep learning method. *Phys. Fluids* **2022**, *34*, 015111. [CrossRef]
21. Patankar, S.V.; Spalding, D.B. A calculation procedure for heat, mass and momentum transfer in three-dimensional parabolic flows. *Int. J. Heat Mass Transf.* **1972**, *15*, 1787–1806. [CrossRef]
22. Siemens. *STAR-CCM+ User Guide Version 16.04*; Siemens: New York, NY, USA, 2016.
23. Breuer, M. Large eddy simulation of the subcritical flow past a circular cylinder: Numerical and modeling aspects. *Int. J. Numer. Methods Fluids* **1998**, *28*, 1281–1302. [CrossRef]
24. Sohankar, A.; Davidson, L.; Norberg, C. Large eddy simulation of flow past a square cylinder: Comparison of different subgrid scale models. *J. Fluids Eng. Trans.* **2000**, *122*, 39–47. [CrossRef]
25. Kurtulus, D.F. On the unsteady behaviour of the flow around NACA 0012 airfoil with steady external conditions at Re = 1000. *Int. J. Micro Air Veh.* **2015**, *7*, 301–326. [CrossRef]
26. Shrestha, P. Heat Transfer Study of Airfoil Arrays in Low Reynolds Number Gas Flows. Master's Thesis, Auburn University, Auburn, AL, USA, 2020. Available online: http://etd.auburn.edu/handle/10415/7529 (accessed on 17 October 2022).
27. Abadi, M.; Barham, P.; Chen, J.; Chen, Z.; Davis, A.; Dean, J.; Devin, M.; Ghemawat, S.; Irving, G.; Isard, M.; et al. TensorFlow: A System for Large-Scale Machine Learning. In Proceedings of the 12th USENIX Symposium on Operating Systems Design and Implementation (OSDI 16), Savannah, GA, USA, 2–4 November 2016.
28. LeCun, Y.; Bengi, Y.; Hinton, G. Deep learning. *Nature* **2015**, *521*, 436–444. [CrossRef] [PubMed]
29. Kingma, D.P.; Ba, J. Adam: A Method for Stochastic Optimization. In Proceedings of the International Conference on Learning Representations (ICLR), San Diego, CA, USA, 24–28 October 2015.
30. Rumelhart, D.E.; Hinton, G.E.; Williams, R.J. Learning representations by back-propagating errors. *Nature* **1986**, *323*, 533–536. [CrossRef]